Check for updates

Subwavelength resolution scanning diffracted-light microscopy using plasmonic ultra-thin condensers

SUELI SKINNER-RAMOS,[1,2,*] **HIRA FAROOQ,**[1] **HAWRA ALGHASHAM,**[1] **AYRTON A. BERNUSSI,**[2,3] **AND LUIS GRAVE DE PERALTA**[1,2]

[1]*Department of Physics and Astronomy, Texas Tech University, Lubbock, TX 79409, USA*
[2]*Nano Tech Center, Texas Tech University, Lubbock, TX 79409, USA*
[3]*Department of Electrical and Computer Engineering, Texas Tech University, Lubbock, TX 79409, USA*
*s.skinner-ramos@ttu.edu

Abstract: We used a rotating slit placed at the back focal plane of the microscope's objective lens to scan the light diffracted by a plasmonic crystal, which had a period smaller than the resolution limit of the optical microscope. A set of images were collected at different orientations of the slit. A high-resolution image of the plasmonic crystal was obtained by processing the experimental images using a numerical Fourier ptychographic algorithm. Supporting simulations of the experiments are also presented.

1. Introduction

Plasmonic Ultra-Thin Condensers (UTC) with a volume three orders of magnitude smaller than traditional microscope condensers have a numerical aperture $NA_c > 1$ [1,2]. Consequently, optical microscopes with objective lenses with numerical aperture $NA_o > NA_c$, in combination with plasmonic UTCs, have been used for high-resolution optical imaging [1,2]. Moreover, plasmonic UTCs with a very large NA_c could make a novel kind of optical nanoscope possible [2,3]. Plasmonic UTCs illuminate the sample under observation with surface plasmon polaritons (SPP) [4], which are excited by near-field spontaneous fluorescent emission [1,2,5]. The light used for imaging in a plasmonic UTC-microscope arrangement is the leakage radiation associated to the excited SPPs [6], which forms a hollow-cone of light characteristic of ring-shaped condensers when there is no sample in the UTC [1,2,5]. As for any microscope-condenser combination, when $NA_o > NA_c$, the resolution limit of a plasmonic UTC-microscope arrangement is $\sim\lambda/(NA_o + NA_c)$, where λ is the wavelength of the leakage radiation [1,2,7,8]. However, when $NA_c > NA_o$, its resolution limit is the Rayleigh Resolution limit $\lambda/(2NA_o)$ [9,10]. This is because when $NA_c > NA_o$, the spatial frequencies $(1/p)$ associated to the sample structure [11], which are larger than $(NA_o + NA_c)/\lambda$, cannot be collected by a NA_o microscope objective lens [2,3]. The spatial frequencies larger than $(2NA_o)/\lambda$ but smaller than $(NA_o + NA_c)/\lambda$ can be collected by a NA_o objective lens. This makes the Fourier plane imaging microscopy (FPIM) technique which permits the optical detection of periodic structures with a period (p) in the range $\lambda/(NA_o + NA_c) < p < \lambda/(2NA_o)$ possible [12]. However, FPIM is not technically a proper imaging technique because no image of a sample with period (p), where $\lambda/(NA_o + NA_c) < p < \lambda/(2NA_o)$, is formed directly in a camera placed at the microscope's real plane (RP). This is because a NA_o objective lens cannot collect the zero-order diffraction ring of radius $NA_c > NA_o$, which is produced by such periodic structure when it is illuminated by a hollow-cone of light [12]. Nevertheless, phase-recovery microscopy techniques [13–28], such as, Fourier ptychographic microscopy (FPM) permit to obtain a high-resolution image of the sample when $\lambda/(NA_o + NA_c) < p < \lambda/(2NA_o)$ [22,24]. However, FPM requires image diversity to accomplish this achievement. FPM is based on the collection of several low-resolution RP images obtained by illuminating the sample from different directions. Originally, FPM was designed to work only for single illumination-direction acquisition at a time, which required a lot of time to reconstruct a high-resolution

image [22–25]. One way to speed the process up is to illuminate the sample simultaneously from multiple directions at the same time, this technique is named illumination direction multiplexing (IDM) [26–28]. However, in IDM-FPM the sample should be illuminated with a set of different IDM patterns to achieve the required image diversity [27]. Although plasmonic UTCs simultaneously illuminate the sample from multiple directions, it does not provide the necessary image diversity. To overcome this issue, in this work, we inserted a rotating slit placed at the back focal plane of the microscope's objective lens to selectively capture specific directions of the light diffracted by the sample. In general, low-resolution IDM RP images obtained with the slit oriented in different directions are unique; thus providing the required image diversity for the successful convergence of the IDM-FPM algorithm. We called this new technique IDM Scanning Diffracted-Light Microscopy (IDM-SDLM) to emphasize its principal difference to IDM-FPM; i.e., in IDM-FPM a set of different IDM RP images are produced by illuminating the sample with a set of IDM patterns, while in IDM-SDLM a set of different IDM RP images are produced by using different directions of the light diffracted by the sample for imaging. It is worth noting that in contrast to FPIM but similar to IDM-FPM, IDM-SDLM is a phase-recovery imaging technique capable of producing high-resolution images of periodic structures with $\lambda/(NA_o + NA_c) < p < \lambda/(2NA_o)$. IDM-SDLM then opens the doors for subwavelength resolution imaging using a plasmonic UTC-microscope combination with $NA_c > NA_o$. Consequently, as soon as plasmonic UTCs with very large NA_c are demonstrated, a novel kind of optical nanoscope can then be realized using the IDM-SDLM technique [2,3]. The rest of this paper is organized in the following manner: In Section 2 we describe the experimental setup used in this work and the experimental images obtained. Also, an experiment demonstrating the fundamental resolution enhancement concepts using a plasmonic crystal sample. The sample was designed to demonstrate the subwavelength resolution imaging capabilities of the IDM-SDLM technique implemented using a plasmonic UTC-microscope arrangement with $NA_c > NA_o$. In Section 3, we will introduce and describe the IDM-SDLM algorithm, and simulations. We conducted a full simulation of the experiments described in Section 2. A comprehensive study of the IDM-SDLM algorithm, including its applicability to arbitrary samples, will be reported elsewhere. In Section 4, we discuss the results obtained after processing the experimental images with the numerical algorithm discussed in Section 3. Finally, the conclusions are presented in Section 5.

2. Experiments

In this work, we used the experimental setup presented in Fig. 1. We worked with a Nikon Elipse Ti inverted microscope mounted with a numerical aperture $NA_o = 0.65$ collection objective lens and a band-pass spectral filter centered at $\lambda = 570$ nm wavelength with a 10 nm bandwidth. The resolution limit of this microscope arrangement is therefore $\lambda/(2NA_o) = 438.5$ nm.
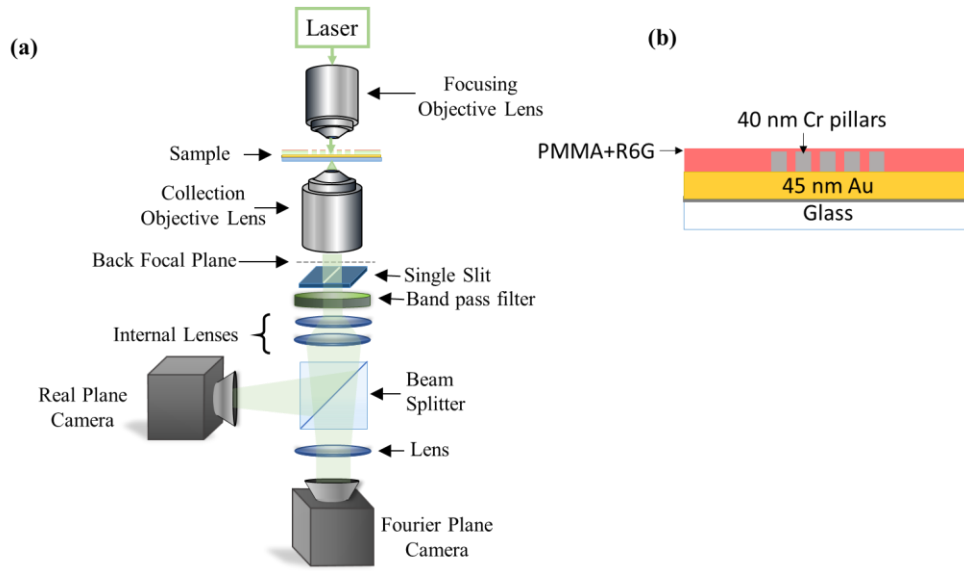
Fig. 1. (a) Schematic illustration of the experimental setup. (b) Cross-sectional schematic of the plasmonic UTC structure with a periodic array of Cr pillars.

As shown in Fig. 1(a), the microscope setup has two charged-couple device (CCD) cameras attached that are used to obtain the RP and FP images of the sample. The sample, a plasmonic crystal with rectangular symmetry [12], is illuminated by a diode laser of wavelength $\lambda = 532$ nm. As shown in Fig. 1(b), the plasmonic crystal consists of 40 nm thick chromium pillars on a 45 nm thick layer of gold, that is adhered to a glass coverslip substrate by a 2nm thick chromium layer. The chromium pillars constitute the structures to be imaged by the optical system. The sample was fabricated using electron beam evaporation technique to deposit the adhesion chromium and gold layers. The chromium pillars were made by depositing chromium using e-beam evaporation on a PMMA-A6 resist mask having the pillar arrangement lithographically defined. The pillar structure is laid out in a rectangular lattice arrangement with periods $p_x = 940$ nm and $p_y = 360$ nm. As shown in Fig. 1(b), the structure of the plasmonic UTC also includes a PMMA layer doped with Rhodamine 6G (fluorescent material), which was deposited on top of the chromium rectangular lattice structure to work as the excitation source of SPPs. The Rhodamine 6G fluorescence emission peak occurs at $\lambda = 570$ nm wavelength when pumped by the $\lambda = 532$ nm wavelength laser. When the surface plasmon polariton is excited at the PMMA/gold interface, a plasmonic UTC with $NA_c = 1.25 > NA_o$ is formed. The spectral filter blocks the direct laser illumination but allows the leakage radiation associated to the excited SPPs to pass. The chromium pillar's periodicity was chosen such that $p_y = 0.360$ μm $< \lambda/(2NA_o)$ is beyond the microscope's diffraction limit, but it is above the theoretical resolution limit of the condenser-microscope set up $\lambda/(NA_o + NA_c) = 0.325$ μm, and the horizontal periodicity $p_x = 940$ nm is easily imaged since $p_x = 0.940$ μm $> \lambda/(2NA_o)$. As sketched in Fig. 1(a), a 0.4 mm wide rotating slit, which corresponds to a numerical aperture width ($W_S = 0.2$) in the microscope's FP, was placed in the back focal plane of the collection objective lens. The slit selectively transmits specific emission directions of the leakage radiation associated to the SPPs that interacted with the chromium structure on the UTC.

Nine pairs of IDM FP-RP images corresponding to different slit orientations were acquired. The slit orientation was varied from 0 to 180 degrees at 20 degrees angle increments, where the zero-degree angle orientation corresponds to the slit oriented along the direction of pillars having the larger period p_x. To compensate for the reduction of the light throughput, resulting from the insertion of the slit into the optical path, the camera exposure

time was increased from approximately 600 ms (no slit) to up to 6 s with the slit in place. Figure 2 shows some examples of the pairs of FP-RP images obtained with the experimental set up sketched in Fig. 1(a).
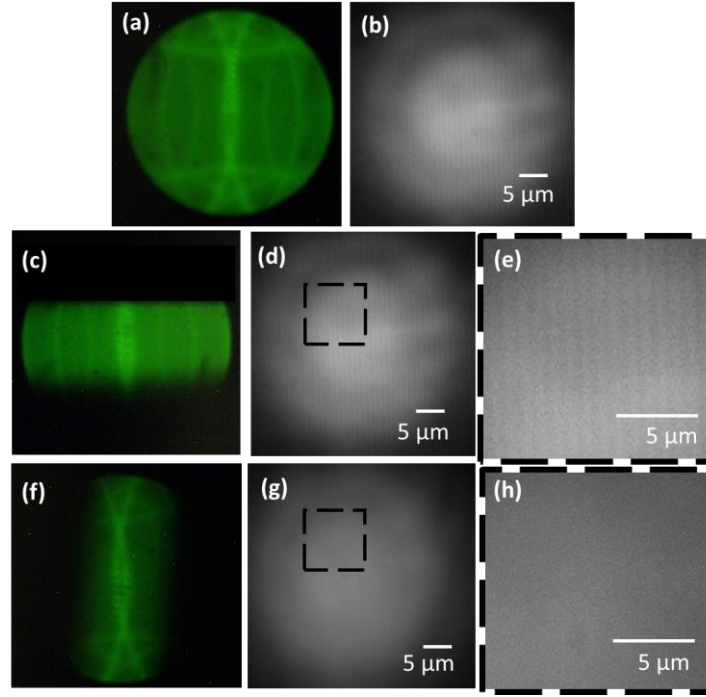

Fig. 2. Experimental (a) FP and (b) RP images of the sample obtained without the slit. Typical examples of experimental pairs of (c, f) FP and (d, g) RP images obtained with the slit at the back focal plane of the objective lens oriented (c-d) perpendicularly to the sample's periodicity with p_x = 940 nm, and (f-g) after rotating the slit at an angle of 80 degrees. (e) and (h) Images obtained after zooming in the square regions shown in (d) and (g), respectively.

Figures 2(a) and 2(b) are the FP and RP images of the sample, respectively, that were obtained without the slit placed at the back focal plane of the objective lens. The bright arcs observed in the IDM FP image shown in Fig. 2(a) are characteristic signatures of IDM FP images obtained by illuminating a sample with a ring-shaped condenser [1,2,12]. The vertically oriented arcs in Fig. 2(a) correspond to fractions of several high-order diffraction rings produced by the larger periodicity of the sample. In correspondence, and as expected because p_x = 940 nm > $\lambda/(2NA_o)$ = 438 nm, the largest periodicity of the sample is visible in the IDM RP image shown in Fig. 2(a). In contrast, only two horizontally oriented arcs are observed in Fig. 2(a). They correspond to fractions of the first-order diffraction rings produced by the smallest periodicity of the sample. The zero-order diffraction ring is not visible in Fig. 2(a) because $NA_c > NA_o$. In excellent agreement, and as anticipated because p_y = 360 nm < $\lambda/(2NA_o)$, the smallest periodicity of the sample is not visible in Fig. 2(a). Nevertheless, the presence of the horizontal oriented arcs in Fig. 2(a) demonstrates the existence of information about the smallest periodicity of the sample in the IDM FP shown in Fig. 2(a), and consequently in the IDM RP image shown in Fig. 2(d). FPIM permits to detect the presence of the smallest periodicity of the plasmonic crystal using the IDM FP image [12]. The information about the smallest periodicity of the sample is not directly recognizable in the IDM RP image shown in Fig. 2(d). As we will show, the IDM-SDLM technique permits to extract this information from a set of different IDM RP images obtained using the experimental set-up sketched in Fig. 1. The pair of experimental FP-RP images shown in Fig. 2(c) and Fig. 2(d) were obtained with the slit oriented at Θ = 0 degrees; i. e., with the slit

oriented perpendicular to the largest periodicity of the sample. In the IDM FP image shown in Fig. 2(c), only fractions of bright vertically-oriented arcs can be seen; this means that the slit at this orientation blocked the diffracted-light directions corresponding to the horizontally oriented arcs seen in Fig. 2(a). In excellent agreement, only the largest sample's periodicity can be seen in the IDM RP image shown in Fig. 2(d), and in its inset shown in Fig. 2(e). The IDM FP and RP images shown in Fig. 2(f) and Fig. 2(g), respectively, were obtained by rotating the slit 80 degrees. In this case, as shown in Fig. 2(h), which is an inset of Fig. 2(g), no periodicities are visible. This in correspondence with the presence in the IDM FP image of a single pair of bright arcs oriented in both vertical and horizontal directions, shown in Fig. 2(f). Scanning the directions of the leakage radiation with the rotating slit then resulted in different IDM RP images. Without the slit, only the IDM RP image shown in Fig. 2(b) can be collected. However, by rotating the slit placed at the back focal plane of the objective lens, the image diversity required for the successful convergence of the IDM-SDLM algorithm can be achieved.

3. IDM-SDLM algorithm and simulations

Figure 3 shows a simplified flowchart of the IDM-SDLM algorithm, which is similar to the IDM-FPM algorithm [26–28].
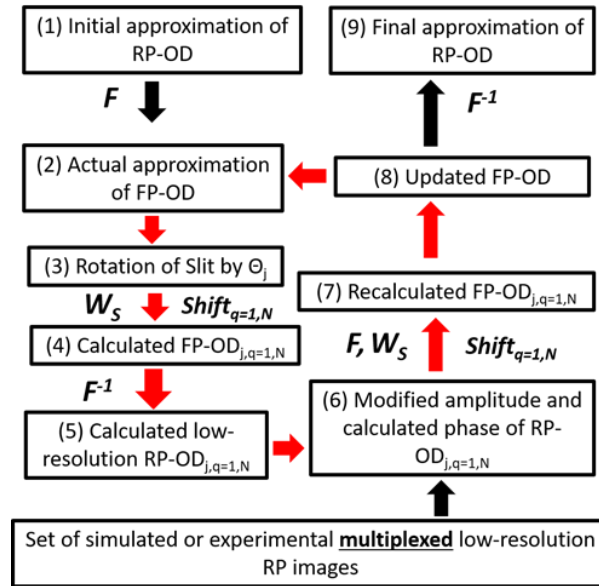

Fig. 3. Flowchart of the IDM-SDLM algorithm.

IDM-SDLM algorithm can recover the unmeasured phase from a set of low-resolution IDM RP images as described in Section 2. As shown in block (1) of Fig. 3, the IDM-SDLM algorithm starts by assuming an initial approximation for the amplitude ($a_{m=0}(r)$) and phase ($p_{m=0}(r)$) of the Real Plane - Optical Disturbance (RP-OD) [29–31]. Next, as shown in block (2) of Fig. 3, the first actual approximation ($m = 1$, $j = 1$) of the Fourier Plane-Optical Disturbance (FP-OD) is calculated by applying a two-dimensional (2D) Fourier transform operation (F) [26–28]:

$$A_{m,j}^{act}(k)e^{iP_{m,j}^{act}(k)} = F\left[a_{m=0}(r)e^{ip_{m=0}(r)}\right], \tag{1}$$

where r and k are 2D vectors defined in the RP and FP, respectively. A rectangular window $W_S(\Theta_j)$, that corresponds to the physical slit placed at the objective back focal plane is defined in the FP with length NA_o, centered at $k = 0$, and width W_S. As follows in block (3), the

rectangular window is then rotated by an angle Θ_j with respect to $k = 0$. Since the sample is illuminated by a plasmonic UTC from different directions, we can approximate this process by considering the sample simultaneously illuminated from N different directions, for any given slit orientation, within the directions defined by the FP vectors k_q, where $q = 1, 2, ..., N$. Thus, as represented by the block (4) in Fig. 3, not one, but an N number of FP-OD$_{j,,q}$ corresponding to a singular slit orientation Θ_j must be calculated, one for each direction of illumination q, using the following equation [26–28]:

$$A_{m,j,q}(k)e^{iP_{m,j,q}(k)} = A_{m,j}^{act}(k-k_q)e^{iP_{m,j}^{act}(k-k_q)} \cdot W_S(\Theta_j). \tag{2}$$

This equation should be evaluated N times for each slit orientation Θ_j; the actual approximation of the FP-OD should be shifted each time by k_q and then multiplied by the rotated rectangular window $W_S(\Theta_j)$. Once the first approximation to the amplitude and phase corresponding to the FP image is calculated, then we can proceed to block (5) where the amplitude ($a_{m,j,q}(r)$) and phase ($p_{m,j,q}(r)$) corresponding to the related RP image are calculated by applying a 2D inverse Fourier transform operation (F^{-1}) using the following expression [26–28]:

$$a_{m,j,q}(r)e^{ip_{m,j,q}(r)} = F^{-1}\left[A_{m,j,q}(k)e^{iP_{m,j,q}(k)}\right]. \tag{3}$$

As shown in the block (6), exactly as the IDM-FPM algorithm [26–28], in IDM-SDLM, the calculated amplitude of each low-resolution RP image ($a_{m,j,q}(r)$) is modified using the following equation:

$$a_{m,j,q}^{\mathrm{mod}}(r) = \sqrt{\frac{I_{RP,j}}{I_{RPT}}}a_{m,j,q}(r),$$

$$I_{RPT} = \sum_{q=1}^{N} I_{RP,j,q}, \quad I_{RP,j,q} = [a_{m,j,q}(r)]^2, \tag{4}$$

where $I_{RP,j}$ is the intensity of the experimental (or simulated) multiplexed low-resolution RP image number j, which was obtained with the slit oriented at Θ_j. It should be noted that in IDM-FPM, a set of different $I_{RP,j}$ are obtained by changing the pattern of IDM [26–28], while in IDM-SDLM different $I_{RP,j}$ are obtained by rotating de slit. Then, as shown in the block (7), each FP-OD$_{j,q}$ is recalculated using the following equation [26–28]:

$$A_{m,j,q}^{rec}(k)e^{iP_{m,j,q}^{rec}(k)} = F\left[a_{m,j,q}^{\mathrm{mod}}(r)e^{ip_{m,j,q}(r)}\right] \cdot W_S(\Theta_j. \tag{5}$$

As shown in the block (8), the updated approximation of the FP-OD with NA_s is calculated by adding a weighted difference between calculated and recalculated FP-ODs with NA_o to the actual approximation of the FP-OD given by Eq. (1); i.e., using Eq. (6) [26–28]:

$$A_{m,j}^{upd}(k)e^{iP_{m,j}^{upd}(k)} = A_{m,j}^{act}(k)e^{iP_{m,j}^{act}(k)}$$

$$+ \alpha \sum_{q=1}^{N}\left[\gamma A_{m,j,q}^{rec}(k+k_q)e^{iP_{m,j,q}^{rec}(k+k_q)} - \beta A_{m,j,q}(k+k_q)e^{iP_{m,j,q}(k+k_q)}\right]. \tag{6}$$

After the initial approximation of the FP-OD is updated, this new image is used as the actual approximation ($j = 2$), as shown by the arrow from block (8) to block (2). The operations connected by red arrows in Fig. 3, are continuously performed for each slit orientation (indicated by the sub-index j). This constitutes the first iteration ($m = 1$) in the IDM- SDLM algorithm, and the algorithm should converge after several iterations. Finally, as shown in block (9), the 2D Fourier transform of the FP-OD gives the final RP-OD.

We performed a full simulation of the experiment described in Section 2 using nine simulated IDM low-resolution RP images corresponding to the nine experimental RP images obtained with the experimental set up sketched in Fig. 1(a). The plasmonic UTC was approximated by $N = 18$ discrete sources of planar waves forming a ring with $NA_c = 1.25$. The simulated IDM images were calculated assuming a known OD at the sample's plane followed by using Eqs. (1), (2) and (3), as indicated by the blocks (1) to (5) in Fig. 3. Then the simulated IDM RP images [I_{RPT} in Eq. (4)] were calculated as the sum of the intensities corresponding to the N calculated RP-ODs [$I_{RP,j,q}$ in Eq. (4)]. As expected, a good correspondence was observed between the simulated IDM RP images and the corresponding experimental images. The IDM-SDLM algorithm starts by assuming an initial approximation of the RP-OD. As it is often chosen in IDM-FPM [26–28], we used $p_{m=0}(r) \equiv 0$ and $a_{m=0}(r)$ as the amplitude corresponding to a low-resolution RP image obtained with the same experimental set up but without the slit. However, when a periodic sample is illuminated, a better RP-OD initial approximation can be obtained by extracting the information contained in the experimental (or simulated) FP images using the FPIM technique [12]. Therefore, we constructed the initial approximation of the RP-OD with $p_{m=0}(r) \equiv 0$ and $a_{m=0}(r)$ given by the following equation [29]:

$$a_{m=0}(r) = c_1 \sqrt{I_{RP,\perp}} + c_2 \sqrt{I_{RPIM}}, \qquad (7)$$

where c_1 and c_2 are arbitrary constants, I_{RPIM} is the intensity of the RP image that could be obtained by processing the experimental FP images using the FPIM technique [12, 29], and $I_{RP,\perp}$ is the intensity of a RP image obtained with the experimental set up sketched in Fig. 1(a) without the slit. If we set $c_2 = 0$, Eq. (7) corresponds to the initial approximation used in IDM-FPM. As shown in Figs. 4(a) to 4(d), FPIM detects periodic structures with a period smaller than the Rayleigh resolution limit by extracting useful information present in the experimental FP images [12, 29].
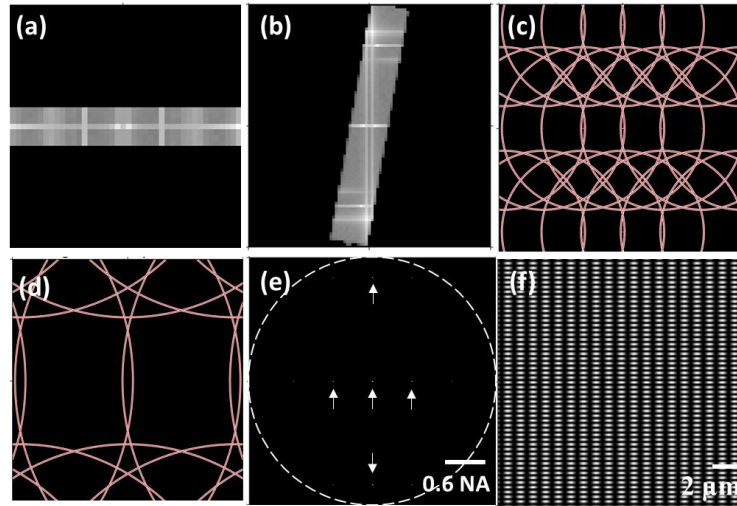

Fig. 4. (a-b) Instances of simulated IDM FP images corresponding to $\Theta_j = $ (a) 0 and (b) 80 degrees. (c-f) Results obtained after processing the nine simulated FP images of the sample using the FPIM technique. (c) Diffraction rings of radii equal to $NA_c = 1.25$, (d) fraction of the first-order diffraction rings visible with $NA_o = 0.65$ objective lens, (e) respective centers of the diffraction rings separated by a distance $\lambda/p_x = 0.6$, and $\lambda/p_y = 1.6$ and, (f) I_{FPIM}.

Figures 4(a) and 4(b) show two instances of simulated IDM FP images corresponding to the slit oriented at $\Theta_j = 0$ and 80 degrees, respectively. As expected, they closely match the experimental images shown in Figs. 2(c) and 2(f), respectively. Similar to the experimental

IDM FP images shown in Figs. 2(c), and 2(f), the simulated IDM FP images seem to rotate, forming a ring of radius NA_c that corresponds to the ring-like illumination provided by plasmonic UTCs. As shown in Fig. 4(c), the FPIM technique allows for the reconstruction of the zero- and higher-orders diffraction rings that would be formed in a microscope's FP, if the sample was illuminated by a ring-shaped condenser, and observed using a hypothetical objective lens with very large numerical aperture. The solid arcs seen in Fig. 4(d), which match the bright arcs visible in Fig. 2(a), are the portions of the first-order diffraction rings with radii equal to NA_c seen in Fig. 2(c) that can be captured with the $NA_o = 0.65$ objective lens. The centers of the zero- and first-order diffraction rings separated by a distance $\lambda/p_x =$ 0.6, and $\lambda/p_y = 1.6$ (in numerical aperture units) are indicated by the arrows shown in Fig. 4(e). This figure represents the diffraction pattern observable under perpendicular illumination with an objective lens having a synthetic numerical aperture $NA_s = NA_o + NA_c =$ 1.9, which is represented by the discontinuous-line ring in Fig. 4(e). Figure 4(f) shows I_{RPIM}, which was obtained by taking the Fourier transform of Fig. 4(e). It is worth noting that I_{RPIM} contains both periodicities of the sample, as clearly seen in Fig. 4(f), but it is not an image of the sample. This is because FPIM is not a proper imaging technique but a detection one [13, 32]. In the simulations of the experiments described in Section 2, we used Eq. (7) with I_{RPIM}, as shown in Fig. 4(f), as the initial approximation of the RP-OD in the IDM-SDLM algorithm. Figure 5 shows the simulation results that were obtained by processing with the IDM-SDLM algorithm the nine previously simulated low-resolution IDM RP images.
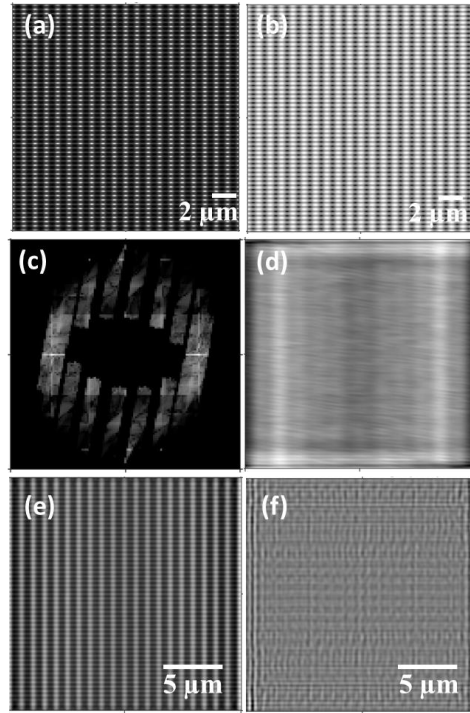

Fig. 5. IDM-SDLM simulation results. Exact (a) amplitude and (b) phase of the RP-OD. (c) Sampled region of the FP and (d) simulated low-resolution IDM RP image obtained when the slit oriented at $\Theta = 80$ degrees. (e) Amplitude and (f) phase of the simulated RP-OD obtained after 10 iterations of the IDM-SDLM algorithm.

Figures 5(a) and 5(b) show the assumed exact amplitude and phase of the RP-OD, respectively, corresponding to our rectangular lattice sample with periods $p_x = 940$ nm, and $p_y = 360$ nm, that could be observed by using a hypothetical objective with a synthetic numerical aperture $NA_s = NA_o + NA_c = 1.9$ when SPPs are excited on the plasmonic UTC.

Figure 5(c) shows the FP region that is sampled by placing the slit at the back focal plane of the objective lens when it is oriented at the angle $\Theta = 80$ degrees. As indicated in Fig. 5(c), this region is formed by a set of $N = 18$ rectangles with a length equal to $NA_o = 0.65$ and a width of 0.2 numerical aperture units. The rectangles are centered at the illumination directions k_q, $q = 1, 2, …, N$ forming a ring of radius $NA_c = 1.25$. Figure 5(d) shows an instance of simulated low-resolution IDM RP image, which was obtained assuming the slit was placed at the back focal plane of the objective lens, and oriented at the angle $\Theta = 80$ degrees. When the slit is rotated, a different FP region is sampled by the slit; consequently, a different low-resolution IDM RP image is obtained. This produces the required image diversity for the convergence of the numerical algorithm. Figures 5(e) and 5(f) show the amplitude and phase, respectively, of the RP-OD obtained by processing the nine simulated IDM RP images, after just 10 iterations of the IDM-SDLM algorithm. A direct comparison of Figs. 5(e) and 5(a) reveals that IDM-SDLM is capable of resolving structures beyond the Rayleigh resolution limit.

4. IDM-SDLM processing of experimental images and discussion

We processed the experimental images following the same procedure described in Section 3. The results obtained using the FPIM techniques, and the experimental FP images obtained with the experimental setup described in Section 2, are shown in Fig. 6.
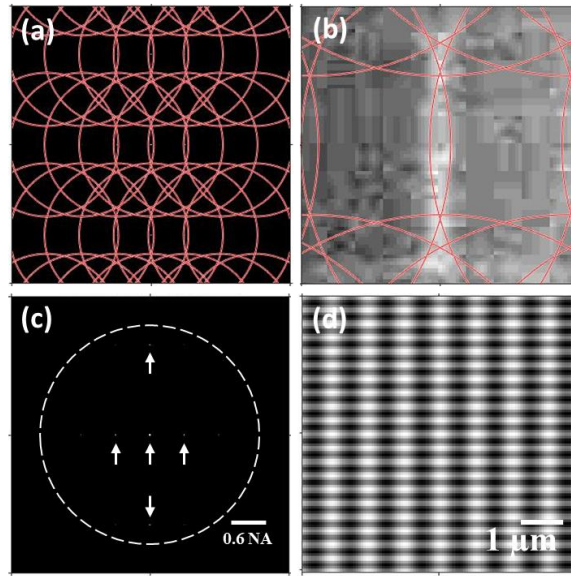

Fig. 6. Results obtained after processing with the FPIM technique the nine experimental FP images (a) Diffraction rings with radius equal to $NA_c = 1.25$, (b) superposition of the sum of all FP images and the first-order diffraction rings, (c) centers of the diffraction rings separated by a distance $\lambda/p_x = 0.6$, and $\lambda/p_y = 1.6$. (d) Amplitude square of the Fourier transform of (c) containing both periodic structures with $p_x = 940$ nm and $p_y = 360$ nm.

As shown in Fig. 6(a), the FPIM technique can generate the diffraction rings that would be visible in the FP images produced if the sample was illuminated by a NA_c plasmonic UTC, and imaged by a hypothetical objective lens with a very large numerical aperture [12, 29]. The radius of the diffraction rings is equal to the plasmon condenser with $NA_c = 1.25$, and their centers are separated in the horizontal and vertical directions by a distance $\lambda/p_x = 0.6$, and $\lambda/p_y = 1.6$ (in numerical aperture units), respectively. As shown in Fig. 6(b), the FPIM technique can determine the value of NA_c from the experimental FP images by adding up all the experimental FP images. The result of the superposition of the experimental FP images can then be compared with the continuous arcs seen in Fig. 6(b), which correspond to the

fraction of the diffraction rings with radius NA_c shown in Fig. 6(a) that are visible using a $NA_o = 0.65$ objective lens. Using this information, Fig. 6(c) is constructed containing the zero- and first-order diffraction spots (indicated by white arrows) within the synthetic numerical aperture (shown by the white dashed circle). Finally, Fig. 6(d) shows the intensity corresponding to the Fourier transform of Fig. 6(c). I_{RPIM} obtained in this way corresponds to a rectangular lattice sample with periods $p_x = 940$ nm and $p_y = 360$ nm. We then used Eq. (7) with I_{RPIM}, as shown in Fig. 6(d), as the initial approximation of the RP-OD in the IDM-SDLM algorithm. We used $c_1 = c_2 = 0.5$, and $I_{RP,\perp}$ was a low-resolution RP image obtained with the set up sketched in Fig. 1(a) but without the slit. Figure 7 shows the results that were produced by processing the nine low-resolution IDM RP images obtained using the experimental set up sketched in Fig. 1, with the IDM-SDLM algorithm.
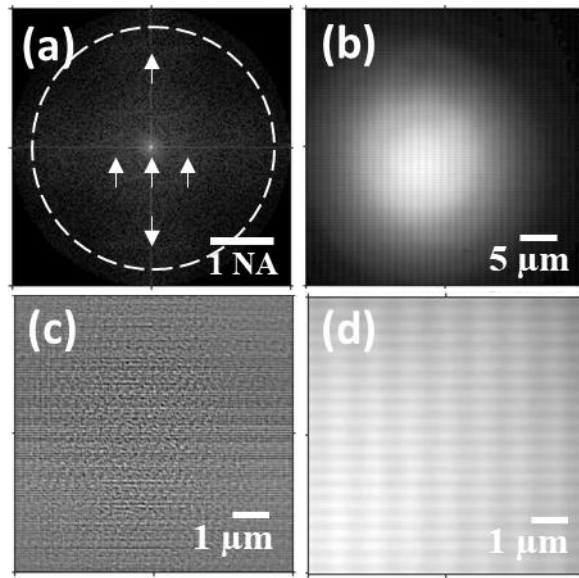

Fig. 7. Results obtained after processing the experimental low-resolution IDM RP images using the IDM-SDLM algorithm. (a) Synthetic FP image with $NA_s = NA_o + NA_c = 1.9$. Amplitude (b) and (c) phase corresponding to the obtained RP- OD. (d) Magnified imaged of (b).

The arrows in Fig. 7(a) point to the zero- and first-order diffraction spots contained in the synthetic FP image, which is delimited by the dashed circle of radius $NA_s = NA_s + NA_c = 1.9$. From Fig. 7(a), we determined a distance between consecutive diffraction spots of ~0.6, and ~1.6, which corresponds to $\lambda/p_x = 0.6$, and $\lambda/p_y = 1.6$, respectively. Figures 7(b) and 7(c) show the amplitude and the phase of the RP-OD, respectively, which were obtained after 10 iterations of the IDM-SDLM algorithm described in Section 3. Both sample's periodicities, with $p_x = 940$ nm and $p_y = 360$ nm, are clearly seen in Fig. 7(d), which is a magnified inset of Fig. 7(b). A comparison between Fig. 7(b) and Fig. 5(e) reveals a good correspondence between the intensity images obtained using the IDM-SDLM algorithm to process experimental and simulated IDM images. In both cases the correct sample structure is revealed. It is important to mention that, as shown in Figs. 2(b), 2(d) and 2(g), the smallest period of the sample is not visible in any of the experimental low-resolution IDM RP images. This demonstrates the IDM-SDLM technique, implemented using a plasmonic UTC-microscope combination with a slit placed at the back focal plane of the objective lens, can image photonic crystals with a resolution beyond the Rayleigh resolution limit. It should be emphasized that IDM-SDLM is an imaging technique. Previously, a photonic crystal with $\lambda/(NA_o + NA_c) < p < \lambda/(2NA_o)$ had been optically detected, but not imaged, using the FPIM

technique and a condenser with $NA_c > NA_o$ [12]. In this work, we have demonstrated a novel optical method for imaging photonic crystals with subwavelength resolution. It should be noted that plasmonic UTCs can be used to image relatively large objects such as human blood cells [2]. The authors of this work will later report simulation results demonstrating successful convergence of the SDLM imaging algorithm for arbitrary samples, which indicates that the presented imaging technique can be applied to a broad range of microscopy applications.

5. Conclusions

We presented a proof-of-concept experiment and simulations that demonstrate enhanced imaging capabilities of plasmonic crystals with periods in the range $\lambda/(NA_o + NA_c) < p < \lambda/(2NA_o)$ using plasmonic UTCs with $NA_c > NA_o$. This achievement was performed using the IDM-SDLM technique, which was implemented using a plasmonic UTC-microscope combination with a rotating slit placed at the back focal plane of the objective lens. Consequently, subwavelength resolution imaging with large field of view of photonic crystal can be realized by using the IDM-SDLM technique in conjunction with plasmonic UTCs having numerical apertures slightly larger than unity, and objective lenses with $NA_o \ll 1$. Moreover, we foresee a novel kind of optical nanoscope based on the use of the demonstrated IDM-SDLM technique and plasmonic UTCs with $NA_c \gg 1$.

Funding

References and links

1. D. B. Desai, D. Dominguez, A. A. Bernussi, and L. de Peralta, "Ultra-thin condensers for optical subwavelength resolution microscopy," J. Appl. Phys. **115**(9), 093103 (2014).
2. L. Grave de Peralta, "Metal slab superlens-negative refractive index versus inclined illumination: discussion," J. Opt. Soc. Am. A **32**(9), 1729–1735 (2015).
3. S. Skinner-Ramos, H. Farooq, H. Alghasham, and L. Grave de Peralta, "Toward phase-recovery optical nanoscopes," Journal of Physical Science and Application **7**, 19–27 (2017).
4. H. Raether, *Surface Plasmons on Smooth and Rough Surfaces and on Gratings* (Springer-Verlag, 1988).
5. I. Gryczynski, J. Malicka, Z. Gryczynski, and J. R. Lakowicz, "Surface plasmon-coupled emission with gold films," J. Phys. Chem. B **108**(33), 12568–12574 (2004).
6. A. Drezet, A. Hohenau, D. Koller, A. Stepanov, H. Ditlbacher, B. Steinberger, F. R. Aussenegg, A. Leitner, and J. R. Krenn, "Leakage radiation microscopy of surface plasmon polaritons," Mater. Sci. Eng. B **149**(3), 220–229 (2008).
7. H. H. Hopkins and P. M. Barham, "The influence of the condenser on microscopic resolution," Proc. Phys. Soc. **63**(10), 737–744 (1950).
8. H. Köheler, "On Abbe's theory of image formation in the microscope," Opt. Acta (Lond.) **28**(12), 1691–1701 (1981).
9. E. Hetcht, *Optics* 3rd ed. (Addison Wesley, 1998).
10. M. Born and E. Wolf, *Principles of Optics* 5th ed. (Pergamon Press, 1975).
11. J. W. Goodman, *Introduction to Fourier Optics* (McGraw-Hill, 1968).
12. D. Dominguez, M. Alhusain, N. Alharbi, A. A. Bernussi, and L. Grave de Peralta, "Fourier plane imaging microscopy for detection of plasmonic crystals with periods beyond the optical diffraction limit," Plasmonics **10**(6), 1337–1344 (2015).
13. D. Sayre, "Some implications of a theorem due to Shannon," Acta Crystallogr. **5**(6), 843 (1952).
14. R. W. Gerchberg and W. O. Saxton, "A practical algorithm for determination of phase from image and diffraction plane pictures," Optik (Stuttg.) **35**, 237–245 (1972).
15. J. R. Fienup, "Reconstruction of an object from the modulus of its Fourier transform," Opt. Lett. **3**(1), 27–29 (1978).
16. J. R. Fienup, "Phase retrieval algorithms: a comparison," Appl. Opt. **21**(15), 2758–2769 (1982).
17. H. M. L. Faulkner and J. M. Rodenburg, "Movable aperture lensless transmission microscopy: A novel phase retrieval algorithm," Phys. Rev. Lett. **93**(2), 023903 (2004).
18. J. M. Rodenburg, A. C. Hurst, A. G. Cullis, B. R. Dobson, F. Pfeiffer, O. Bunk, C. David, K. Jefimovs, and I. Johnson, "Hard-x-ray lensless imaging of extended objects," Phys. Rev. Lett. **98**(3), 034801 (2007).
19. M. J. Humphry, B. Kraus, A. C. Hurst, A. M. Maiden, and J. M. Rodenburg, "Ptychographic electron microscopy using high-angle dark-field scattering for sub-nanometre resolution imaging," Nat. Commun. **3**(1), 730 (2012).

20. A. M. Maiden, J. M. Rodenburg, and M. J. Humphry, "Optical ptychography: a practical implementation with useful resolution," Opt. Lett. **35**(15), 2585–2587 (2010).
21. A. M. Maiden, M. J. Humphry, F. Zhang, and J. M. Rodenburg, "Superresolution imaging via ptychography," J. Opt. Soc. Am. A **28**(4), 604–612 (2011).
22. G. Zheng, R. Horstmeyer, and C. Yang, "Wide-field, high-resolution Fourier ptychographic microscopy," Nat. Photonics **7**(9), 739–745 (2013).
23. S. Dong, Z. Bian, R. Shiradkar, and G. Zheng, "Sparsely sampled Fourier ptychography," Opt. Express **22**(5), 5455–5464 (2014).
24. X. Ou, R. Horstmeyer, G. Zheng, and C. Yang, "High numerical aperture Fourier ptychography: principle, implementation and characterization," Opt. Express **23**(3), 3472–3491 (2015).
25. K. Guo, Z. Bian, S. Dong, P. Nanda, Y. M. Wang, and G. Zheng, "Microscopy illumination engineering using a low-cost liquid crystal display," Biomed. Opt. Express **6**(2), 574–579 (2015).
26. S. Dong, R. Shiradkar, P. Nanda, and G. Zheng, "Spectral multiplexing and coherent-state decomposition in Fourier ptychographic imaging," Biomed. Opt. Express **5**(6), 1757–1767 (2014).
27. L. Tian, X. Li, K. Ramchandran, and L. Waller, "Multiplexed coded illumination for Fourier Ptychography with an LED array microscope," Biomed. Opt. Express **5**(7), 2376–2389 (2014).
28. M. Alotaibi, S. Skinner-Ramos, A. Alamri, B. Alharbi, M. Alfarraj, and L. Grave de Peralta, "Illumination-direction multiplexing Fourier ptychographic microscopy using hemispherical digital condensers," Appl. Opt. **56**(14), 4052–4057 (2017).
29. H. Farooq, S. Skinner-Ramos, H. Alghasham, and L. de Peralta, "Improving the resolution of an optical microscope using ring-like illumination and scanning the direction of the diffracted light with a slit," Opt. Commun. **426**, 201–205 (2018).